energies

Article

An Evaluation Method of Brittleness Characteristics of Shale Based on the Unloading Experiment

Xiaogui Zhou [1], Haiming Liu [1,*], Yintong Guo [2], Lei Wang [2], Zhenkun Hou [3] and Peng Deng [4]

1 Yunnan Key Laboratory of Disaster Reduction in Civil Engineering, Faculty of Civil Engineering and Mechanics, Kunming University of Science and Technology, Kunming 650504, China; xgzhou1002@foxmail.com
2 State Key Laboratory of Geomechanics and Geotechnical Engineering, Institute of Rock and Soil Mechanics, Chinese Academy of Sciences, Wuhan 430071, China; ytguo@whrsm.ac.cn (Y.G.); lwang@whrsm.ac.cn (L.W.)
3 Guangzhou Institute of Building Science Co., Ltd., Guangzhou 510440, China; zhenkunhoucqu@163.com
4 State Key Laboratory for Coal Mine Disaster Dynamics and Control, Chongqing University, Chongqing 400044, China; rocdeng666@163.com
* Correspondence: haiming0871@163.com; Tel.: +86-138-8801-5288

Received: 9 April 2019; Accepted: 6 May 2019; Published: 10 May 2019

Abstract: Shale reservoir has an initial unloading effect during the natural uplift and erosion process, which causes the shale brittleness to change, affecting the design of the fracturing scheme. To consider this, the axial compression loading and confining pressure unloading experiment of shale is carried out, and then the influence of unloading rate on the mechanical parameters, failure characteristics, and the brittleness of rock are analyzed. What is more, a new evaluation method of brittleness characteristics that take the unloading effect into consideration is proposed. The conclusions are as follows: (1) The unloading rate has a weakening effect on the mechanical parameters, such as the destructive confining pressure and the residual strength of the samples. (2) The failure characteristics of shale specimens are a single shear failure in an oblique section under low unloading rate, and multiple shear zones accompanied with bedding fracture under high unloading rate. (3) The brittleness of shale samples is well verified by the brittleness index B_{d1} and B_{d2} during the loading path; nevertheless, it has shortage at the unloading path. This paper proposes a new brittleness evaluation method which can consider the influence of the different unloading rates and unloading points. Furthermore, there is a nice characterization between the brittleness damage and this method.

Keywords: shale; unloading rate; brittleness evaluation; failure characteristics; mechanical parameters

1. Introduction

In recent years, with the further steady growth of gross domestic products, people's demand for energy has become increasingly intense, and the exploration and development of various unconventional energy sources have been gradually advancing. As a kind of clean, efficient, low-carbon unconventional natural gas mineral energy source, shale gas has tremendous reserves and vast distribution regions in China [1,2]. At present, China's shale gas exploration and exploitation are in a stage of rapid development, with various development wells obtaining high-yield natural gas streams, showing favorable prospects for shale gas exploration and exploitation [3]. What is more, China has drilled more than 600 shale gas wells from 2011 to 2016, and shale gas is projected to account for more than 40% of the country's total natural gas production by 2040, which would make China the second-largest shale gas producer in the world after the United States [4].

With the transition of historical time, the shale reservoir has experienced a multi-period geological structure movement, and the formation has experienced the exfoliation and uplift, that is, the local reservoir has undergone the natural unloading process [5,6]. For instance, marine shale in southern China has undergone multi-stage tectonic movements, including land mass cracking-discretization-polymerization, local uplift and erosion, complex storage conditions, and shale gas control factors and richness in different regions [7]. The law of enrichment is unclear. These problems restrict the exploration and exploitation of marine shale gas in China, whose exploration potential and favorable targets of shale gas need to be implemented. The southern marine shale in some parts of China has a self-generated, self-storing, and self-covering mode of accumulation, so the rock is both a reservoir and a cap rock [8]. Therefore, the indoor triaxial unloading mechanical test of shale and the in-depth study of the mechanical properties of rock are of great significance for the evaluation of regional brittleness, airtightness as well as the exploration and development of shale gas.

Many scholars at home and abroad have conducted in-depth research on the mechanical unloading properties of rocks and the evaluation of caprock brittleness and tightness. From the perspective of rock mechanics and numerical simulation, Dewhurst et al. [9] and Lewis et al. [10] discussed the closure of cap rock, respectively. Hermanrud et al. [11], Teige et al. [12], Ogata et al. [13], and Shukla et al. [14] considered that cap thickness, stress, porosity water, saturation, crack occurrence, etc., are related to caprock leakage. Ingram et al. [15] proposed that the uplifting and denudation process would cause the cap rock to transform from plastic to brittle, and at the same time convert from effective closure to leakage.

Therefore, the uplift and erosion of the cap layer are of great significance to the mechanical properties of the caprock. Moreover, it is necessary to carry out the study of the unloading mechanics of the rock. Regarding the mechanical unloading properties of rock, Swansson and Brown [16] studied the fracture development of several kinds of rocks under the unloading path and built special test equipment to control the path effectively. Shimamoto [17] discovered and proposed a new method of the confining pressure unloading test, and analyzed the rock friction strength under different confining pressures. Viktorov et al. [18] detected the wave velocity of rock mass before and after unloading and finds that the longitudinal wave velocity of rock mass decreases after unloading, and the wave velocity changes with time. Lau and Chandler [19] found that the test under the unloading path was more consistent with the engineering practice, and the rock mechanics parameters measured by this test were more accurate. Huang et al. [20] studied the macroscopic and microscopic fracture characteristics of the unloading rupture surface of marble and explained the failure mode from the perspective of fracture, which provided the reference for Jinping Hydropower Station.

In terms of the different rocks, Huang et al. [21], Zhang et al. [22], and Lv et al. [23] analyzed the unloading strength of mudstone, limestone, and granite, respectively. Based on the prediction of rock burst and rock mass safety, Wu et al. [24] investigated the application of rock mass rapid unloading model and applied this model to the engineering. He et al. [25] examined the fracture mechanism of rock under multiaxial stress from the perspective of auxiliary systems such as scanning electronic microscopy (SEM) and acoustic emission (AE) technology, which had a particular reference value for on-site observation. Huo et al. [6] carried out the triaxial unloading mechanics test of mud shale under different confining pressures, and the lateral compression coefficient was proposed to evaluate the tightness of the caprock.

The above studies have carried out unloading tests and sealing evaluation studies on marble, limestone, mudstone, and sandstone from different angles; however, there are few articles published on the mechanical properties of shale under different unloading rates. In the process of exploration and development, block evaluation, as well as block optimization of marine shale in the south, it is necessary to consider that the shale reservoir undergoes multiple stages of the geological movement, the fault is relatively developed, the structural characteristics are different, and the storage conditions are much more complicated. Moreover, due to the tectonic shift, the shale block undergoes natural exfoliation erosion and reservoir uplift, that is, there are natural unloading effects at different rates [7].

Based on this aspect, the three-axis unloading test of shale under high confining pressure is carried out. From the perspective of the exploration of unconventional gas, oil, and rock unloading mechanics, the mechanical properties and damage characteristics of shale under different unloading rates are analyzed. What is more, the brittleness evaluation method based on the unloading elastic modulus E_U and total elastic modulus E_T are proposed, brittleness index B_{d1} and B_{d2} are further optimized, and the rock brittleness characteristics under different unloading rate tests are evaluated by the parameters B_{U1} and B_{U2}, whose feasibility is well verified. These parameters are the technical parameters related to exploration and mining in later block optimization, and the evaluation of shale reservoir sealing and block optimization.

2. Sample Preparation and Test Design

2.1. Triaxial Sample Preparation

The test samples were taken from the fresh outcrop black shale in Jiangkou, Wulong, Chongqing, in China, which is a natural extension of the southern marine shale gas reservoir in Fuling district. The samples were drilled in parallel with the bedding direction, and the cores were sealed and stored in a wax seal to prevent the contact from the air. Then the same rock block was drilled and processed into a standard sample of 50 × 100 mm, perpendicular to the bedding plane in the laboratory, to meet the requirements of the international rock mechanics test procedures [26]. As shown in Figure 1, the diameter tolerance was less than 0.2 mm, the unevenness of the end faces was less than 0.05 mm, and the vertical deviation of the end face from the axis was controlled within ±0.25°.

Figure 1. Part of the samples.

In order to further ensure the homogeneity of the rock samples and reduce the individual differences between them, the rock samples with initial cracks and initial damage were removed by visual observation. Additionally, the rock samples with significant differences in density and wave velocity, beyond 20% of the average value, were removed, and the effective screening of rock samples was realized to meet the accuracy requirements of rock mechanics tests.

2.2. Basic Physical Properties of Shale

Before the shale triaxial unloading experiment, the basic physical properties of the shale were tested. Figure 2 shows the shale mineral diffraction pattern from the X-ray diffraction (XRD), and the primary minerals in the shale can be found as follows. The quartz was 55.9%, illite was 13.11%, albite was 13%, montmorillonite was 8.14%, calcite was 3.77%, pyrite was 3.74%, and dolomite was 2.34%.

The content of brittle minerals in the shale mineral composition is a significant factor determining the gas bearing, airtightness, and fracture ability of shale reservoirs. Generally, if the content of quartz and calcite in the shale is high, the brittleness pf the sample is stronger, and cracks are easily generated under the action of external force. In the process of geological evolution, natural unloading, such as uplifting and denudation, may cause shale gas leakage, which severely affects reservoir brittleness [27].

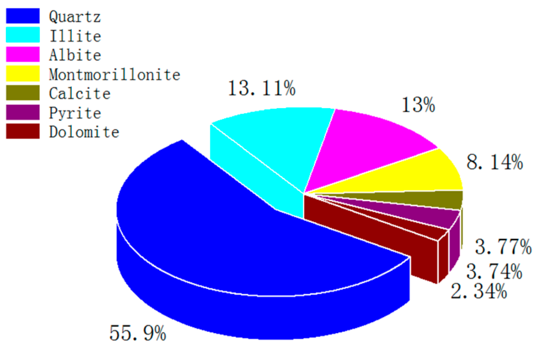

Figure 2. XRD mineral diffraction pattern of the shale sample.

Figure 3 is a microscopic electron micrograph of the shale after magnifying 5000 times and 20,000 times, and the rock samples are characterized by pores of 10 and 2 µm, respectively. The pore size range was between 0.32 and 1.02 µm, and the shale gas was retained in the pores in the adsorption state, which was necessary to study the reservoir in depth and screen the exploration and development of favorable blocks. Therefore, it was of great significance to carry out indoor rock mechanics tests and to understand the mechanical properties of shale.

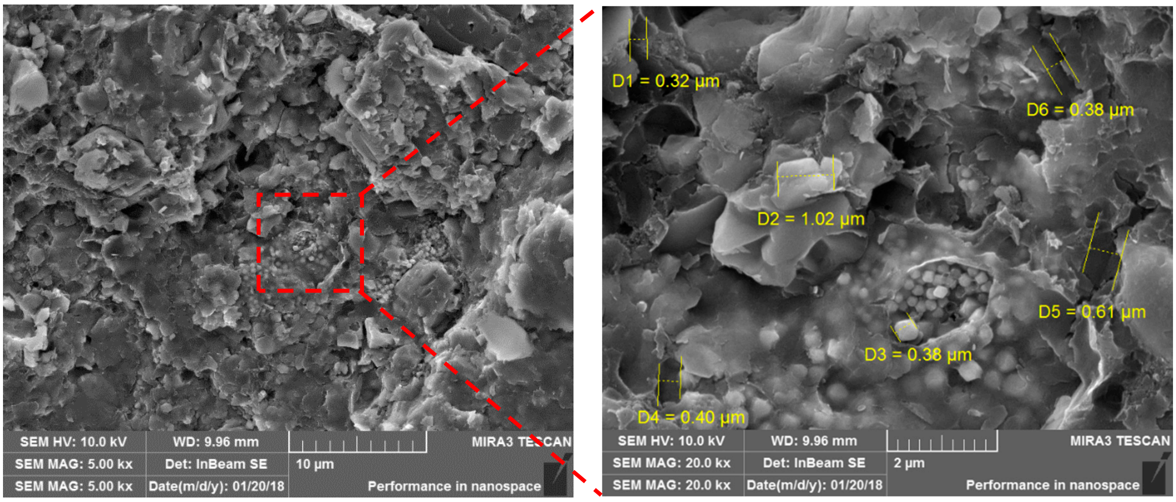

(**a**) 10 µm (**b**) 2 µm

Figure 3. Scanning of microscopic electron microscopy at 10 and 2 µm.

2.3. Conventional Triaxial Compression Test of Shale

Before designing the unloading triaxial compression experiment of shale, we needed to obtain the basic mechanical parameters of shale under conventional triaxial compression in advance to create the experimental unloading parameters. For this reason, the MTS (Mechanics Test System) 815.03 rock triaxial test system was adopted, and the principle of it is shown in Figure 4.

The testing machine comprises a loading part, a testing part, and a control part, whose control part includes a test assistant, a static test software, multifunctional test software, and a function generator control. It can achieve a fully automatic triaxial loading and measurement with full digital control. Based on this system, a conventional triaxial compression test with confining pressures of 0, 20, 40, 60, and 80 MPa was carried out, and the axial strain displacement control method was adopted with the loading rate of 0.001 mm/s.

Figure 5 is a triaxial stress–strain curve of the shale samples, ε_1 represents axial strain, ε_2 represents radial strain and $\sigma_1 - \sigma_3$ represents axial pressure. It can be concluded from the curve that the peak strength and residual strength of the shale sample increase remarkably with the increase of confining pressure, and the elastic modulus and axial strain also increase gradually. The Mohr–Coulomb strength criterion is used to measure the peak strength and confining pressure from Figure 6.

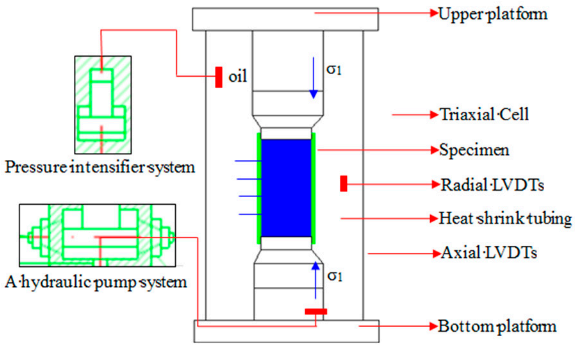

Figure 4. Schematic diagram of the MTS test machine structure.

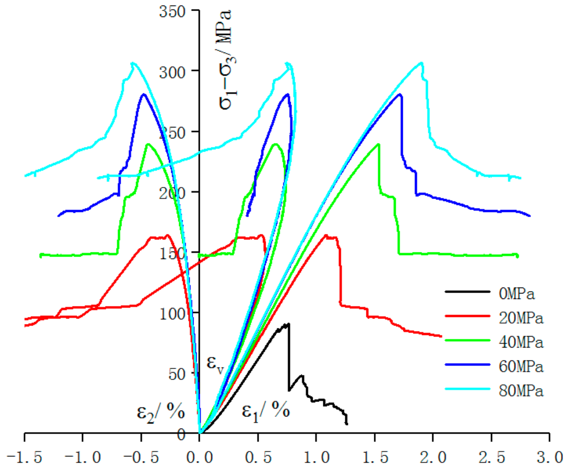

Figure 5. Triaxial stress–strain curve of the samples.

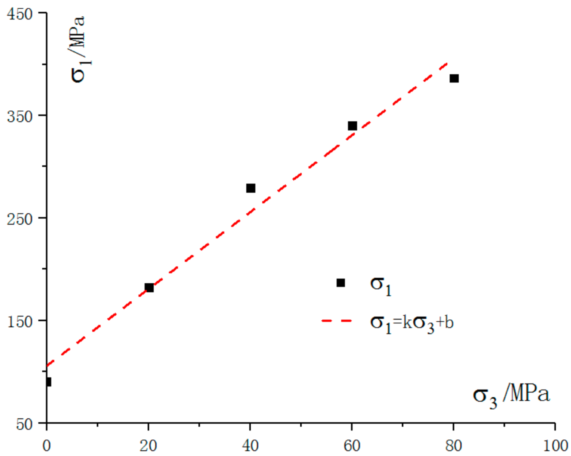

Figure 6. Fitting curve of $\sigma_1 - \sigma_3$.

$$\sigma_1 = k\sigma_3 + b \tag{1}$$

After the curve is fitted, the following equation can be obtained. In Equation (1), k and b are the strength coefficients, which can be expressed by the internal friction angle and cohesion:

$$b = 2c\cos\varphi/(1 - \sin\varphi) \tag{2}$$

$$\begin{aligned} k &= \tan^2(45^\circ + \varphi/2) \\ \varphi &= 35.36^\circ, c = 27.34 \text{ MPa} \end{aligned} \tag{3}$$

where the internal friction angle φ of the rock sample is 35.36°, and the cohesion c is 27.34 MPa, indicating that the shale sample meets the Mohr–Coulomb strength criterion and has a good linear correlation with it. On this basis, the shale three-axis unloading test under different unloading rate conditions was carried out.

2.4. Unloading Test Plan

It can be seen in Figure 6 that under the confining pressure of 60 MPa, the shale sample has no obvious yielding characteristic when the deviatoric stress reaches 80% of the peak intensity, which is 280 MPa. Therefore, 60 MPa is selected as the unloading confining pressure [7], and the stress point at 80% of the peak strength is selected as the unloading point, that is, 224 MPa. The confining pressure was unloaded at a rate of 0.05, 0.1, 0.5, and 1.0 MPa/s, respectively, while maintaining the maximum principal stress the same until the sample was destroyed, reaching the peak of unloading, and then the experiment was stopped after the apparent stress step appeared. The changing of stress during unloading is shown in Figure 7. In particular, the part of the curve with the confining pressure in Figure 8 is a schematic diagram, highlighting the unloading curve. The slope of the real process should be 45°, and the maximum principal stress and the confining pressure increase in proportion.

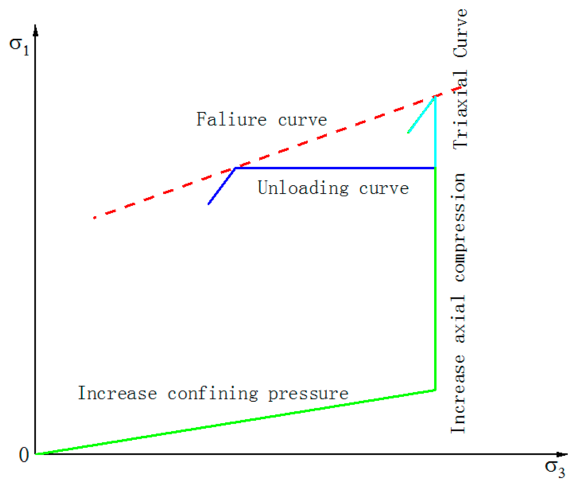

Figure 7. Triaxial unloading curve.

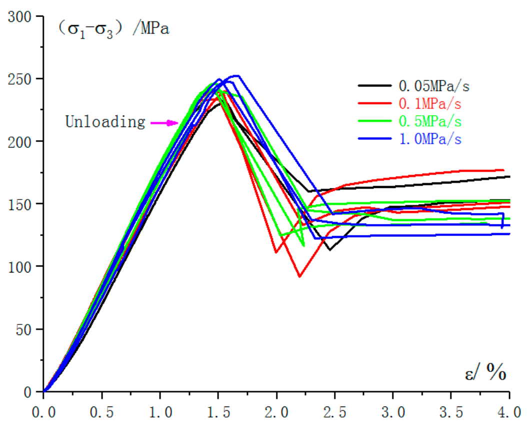

(**a**) Deviatoric stress–strain curve of the unloading.

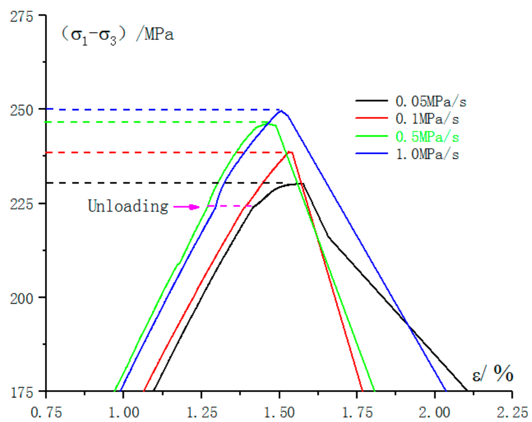

(**b**) Partial amplification curve of (a).

Figure 8. Deviatoric stress–strain curve and partial amplification curve.

3. Analysis of Test Results

3.1. Analysis of Unloading Experiment

3.1.1. Stress–Strain Curve Analysis of Unloading

As shown in Figure 8, the different unloading rate deviatoric stress–strain curves of shale under 60 MPa confining pressure could be divided into compaction section, loading section, unloading section, peak section, and residual section. The compaction stage of shale was more apparent and shows that it had initial damage. Due to the continuous impact of high confining pressure and deviatoric stress, the shale produced noticeable elastic deformation, and the slope tended to be stable after the curve began to enter the loading section. Then at the unloading point, there was a significant unloading section, the curve showed a small amplitude deflection once again, and reached the peak section. It finally entered the residual section and stopped the test.

Before the unloading point, the stress–strain curves of the shale samples were in the elastic stage. After the unloading point, the stress–strain curve showed a significant deflection, deviated from the original straight-line segment, and entered into the next straight-line segment. The slope of the segment was smaller than the initial slope, that is, the deformation modulus of the rock sample decreased. As the deviatoric stress continued to increase, the curve deviated from the second straight line segment and entered the yielding stage. The axial strain also increased further and then came the peak section. The peak value of the shale stress was different under the condition of unloading rate, and the deformation and failure were more rapid than the conventional triaxial test. The deviatoric stress dropped sharply, and the stress slightly increased before the stress–strain curve reached the residual strength, especially at the unloading rate of and 0.5 MPa/s. Due to the increase of the unloading rate, the shale ruptured rapidly, and the confining pressure was too late to crush the broken shale, causing the deviatoric stress to drop too much. Then the broken shale was gradually pressed by the confining pressure, and the deviatoric stress slowly rose to reach the residual strength. Then, the deviatoric stress appeared to be the obvious stress step, the axial strain increased further, and the residual strength at different unloading rates showed a significant difference. The slope was relatively low at 0.05 MPa/s, relatively high at 1.0 MPa/s, and entered into the straight section again. The strength did not change significantly until the end of the test; at last, the test system was stopped.

As shown in Table 1, the unloading rate had a significant effect on the axial strain, radial strain, and peak stress. For axial strain ε_1, as the unloading rate increased, the average, from small to large, rate was 1.7335, 1.7529, 1.648, and 1.837. Although there was a fluctuation, the overall increasing trend was still obvious. When the unloading rate v^* was 1.0 MPa/s, the average value of axial strain reached 1.837%, which was 6.0% higher than 0.05 MPa/s, and the peak value increased by 1.952%. In terms of radial strain, there was a significant increase with the increase in rate. The average value at different rates was 0.2459, 0.316, 0.3662, and 0.4212. The shale tended to rapidly increase in the radial strain under high rate, with an increase of 71.2% compared to 0.05 MPa/s, which was a huge change compared to the increase of 6.0% in axial strain. That is, under unloading conditions, the radial strain increased much more than the axial strain. In terms of volumetric strain, it was 1.246, 1.1253, 0.9157, and 1.102. The volumetric strain showed a decreasing trend with the increase of the unloading rate, which was gradually weakened by the expansion effect.

In the Table 1, $v*$ represents the unloading rate, MPa/s; $\lg(v^*)$ represents the logarithm of unloading rate; $(\sigma_1 - \sigma_3)_{\max}$ represents the maximum axial pressure, MPa; $\lg((\sigma_1 - \sigma_3)_{\max})$ represents the logarithm of maximum axial pressure; $(\sigma_1 - \sigma_3)^*$ represents the residual stress, MPa; $\lg((\sigma_1 - \sigma_3)^*)$ represents the logarithm of residual stress; σ_3^* represents the failure confining pressure, MPa; $\lg\sigma_3^*$ represents the logarithm of failure confining pressure.

Table 1. Experimental plan and related parameters.

Serial Number	Density g/cm^3	ε_1	ε_2	ε_3	σ_3 (MPa)	v^* (MPa/s)	lg(v^*)	$(\sigma_1-\sigma_3)^*_{max}$ (MPa)	$\lg((\sigma_1-\sigma_3)^*_{max})$	$(\sigma_1-\sigma_3)^*$ (MPa)	$\lg((\sigma_1-\sigma_3)^*)$	σ_3^* (MPa)	$\lg(\sigma_3^*)$
RF-1-15	2.54	1.78	0.22	1.33	60	0.05	−1.3	229.73	2.36	165.86	2.22	54.27	1.74
RF-4-11	2.51	1.70	0.27	1.16	60	0.05	−1.3	239.61	2.38	151.70	2.18	44.39	1.65
RF-2-6	2.52	1.68	0.30	1.07	60	0.1	−1	233.42	2.39	148.08	2.17	50.79	1.71
RF-3-3	2.52	1.86	0.38	1.11	60	0.1	−1	239.82	2.38	145.49	2.16	44.92	1.65
RF-4-2	2.52	1.74	0.27	1.19	60	0.1	−1	238.48	2.38	174.39	2.24	46.11	1.66
RF-2-5	2.52	1.64	0.36	0.92	60	0.5	−0.3	241.51	2.38	137.32	2.14	43.09	1.63
RF-3-4	2.53	1.62	0.40	0.81	60	0.5	−0.3	240.82	2.38	151.60	2.18	43.57	1.64
RF-3-5	2.53	1.69	0.34	1.02	60	0.5	−0.3	246.22	2.39	132.95	2.12	38.64	1.59
RF-2-2	2.52	1.95	0.45	1.05	60	1.0	0	252.00	2.40	142.00	2.15	32.76	1.52
RF-2-9	2.52	1.73	0.28	1.17	60	1.0	0	249.63	2.40	132.95	2.12	35.11	1.55
RF-4-5	2.53	1.83	0.51	0.82	60	1.0	0	247.88	2.40	125.00	2.10	36.69	1.57

3.1.2. Comparative Study on the Stress–Strain Curves of Loading and Unloading

The deviatoric stress–strain curves of the 40 and 60 MPa confining pressures in the full-process stress–strain curve of Figure 5 of shale are extracted, and the typical deviatoric stress–strain curves at four unloading rates are selected, which is shown in Figure 9.

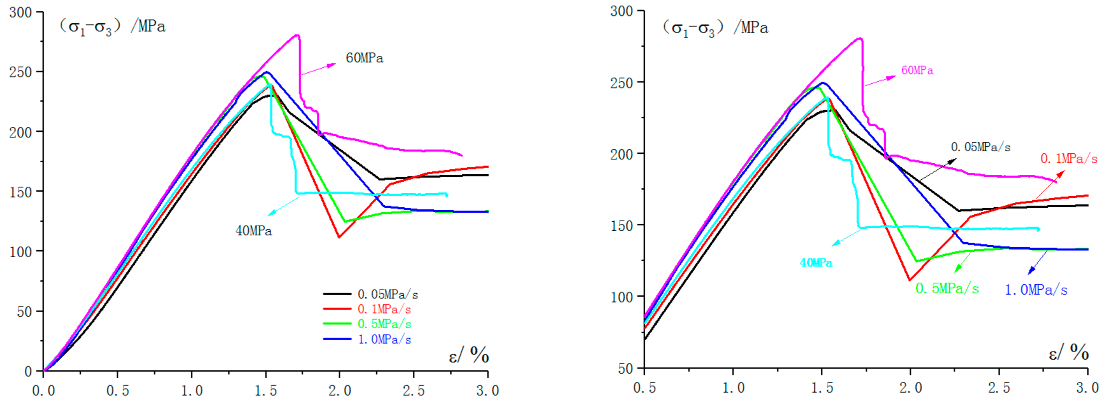

(**a**) Comparison of triaxial loading and unloading stress–strain curves.

(**b**) Partial amplification curve of (a).

Figure 9. Comparison of triaxial loading and unloading stress–strain curves and partial amplification curve.

The unloading stress–strain curve of the 60 MPa confining pressure in Figure 9 shows that it is between the 40 MPa confining pressure and the 60 MPa confining pressure of the triaxial loading test. The stress–strain curve under loading and unloading are entirely different after the peak point. During the triaxial loading test, the peak intensity is higher, and the curve drop rate is faster, the partial stress falls by a large piece when the axial stress changes are tiny. Under the unloading conditions, the peak strength of shale is reduced significantly. At the unloading rate of 0.05 and 0.1 MPa/s, the peak intensity is very close to the peak intensity of 40 MPa loading curve. At the unloading rate of 0.5 and 1.0 MPa/s, the peak intensity is slightly higher than the peak intensity of the 40 MPa loading and less than the peak intensity of the 60 MPa loading. At the same time, the residual strength of the unloading is also reduced. At the unloading rate of 0.05 and 0.1 MPa/s, the residual strength is about 160 MPa, which is higher than the residual strength of 40 MPa loading curve and less than the 60 MPa loading curve. While the unloading rate is 0.5 and 1.0 MPa/s, the residual strength is only about 140 MPa, which is lower than the residual strength under 40 MPa confining pressure, and the curve drop rate is also weakened. That is to say, compared with the loading curve, the unloading has a noticeable weakening effect on the peak strength and residual strength of shale samples. At the same time, there is an excellent relationship between the weakening mechanical parameters and the unloading rate.

3.2. Influence of Unloading Rate on Shale Mechanical Parameters

The peak strength $(\sigma_1-\sigma_3)_{max}$ and residual stress $(\sigma_1-\sigma_3)^*$ are essential parameters in hydraulic fracturing mining. They are important indicators that cannot be ignored in regional airtightness evaluation. As shown in Table 1, the critical analysis of this paper is as follows.

3.2.1. Effect of Unloading Rate on Peak Intensity

Figure 10 is a graph of peak intensity versus unloading rate. Although the peak intensity is discrete, the total increases with the increase of the unloading rate. Under the condition of high unloading rate, the deformation of the shale lags behind the stress, and the partial deformation is too late when the stress reaches a significant value. Thus, the shale exhibits a higher unloading bias stress. In Figure 10, $\log(v^*)$ and $\lg(\sigma_1-\sigma_3)_{max}$ has a significant linear relationship, and are fitted as follows.

$$\lg(\sigma_1-\sigma_3)_{max} = 0.019\lg(v^*) + 2.395, R^2 = 0.95 \quad (4)$$

$$(\sigma_1 - \sigma_3)_{max} = (v^*)^{0.019} + 248.31 \quad (5)$$

The fitting curve shows that $\lg(\sigma_1 - \sigma_3)_{max}$ and $\log(v^*)$ has a significant linear correlation, and the mean is better distributed on the upper and lower sides of the curve. The southern marine shale experienced multiple periods of uplift and erosion, and the shale reservoir gradually discharged once and again. The faster the reservoir is lifted, the higher the deviatoric stress of the internal accumulation, which may be more detrimental to the next exploration and development.

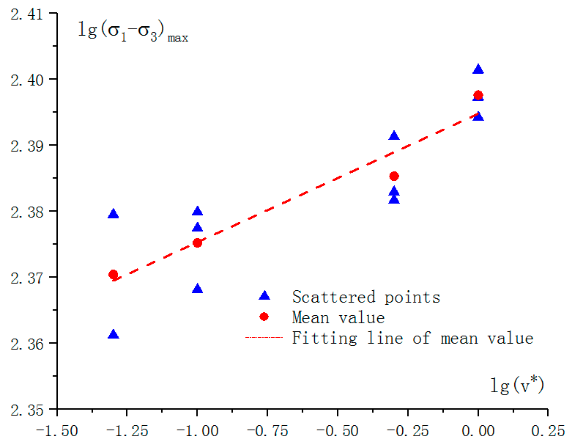

Figure 10. A logarithmic fitting curve of deviatoric stress and unloading rate.

3.2.2. Influence of Unloading Rate on Destructive Confining Pressure

With the increase of the unloading rate v^*, the destructive confining pressure σ_3^* decreases obviously, which is shown in Figure 11. In the geological process, the destructive confining pressure usually corresponds to the overlying stress, which means the overlying stress is becoming smaller and smaller. These parameters are fitted as follows.

$$\lg(\sigma_3^*) = -0.108\lg(v^*) + 1.562, R^2 = 0.91 \quad (6)$$

$$\sigma_3^* = (v^*)^{-0.108} + 36.475 \quad (7)$$

It can be concluded from the fitting curve that σ_3^* and v^* have a significant linear negative correlation, and the mean is also better distributed on the upper and lower sides of the curve. As the unloading rate increases, the performance of the confining pressure is gradually reduced.

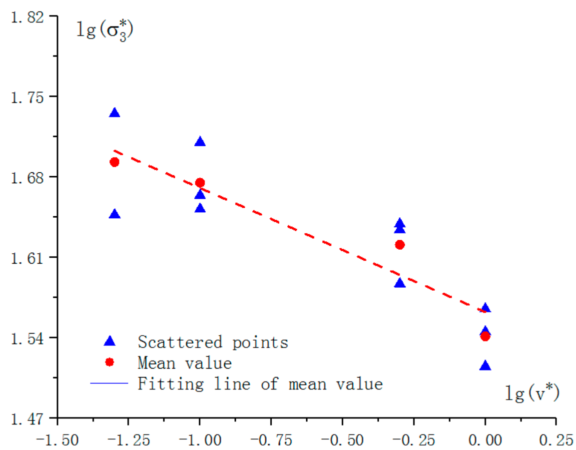

Figure 11. A logarithmic fitting curve of confining pressure and unloading rate.

3.2.3. Effect of Unloading Rate on Residual Stress

Using the data processing method of 3.2.1, as shown in Figure 12, the residual stress $(\sigma_1 - \sigma_3)^*$ and the unloading rate v^* are closely related. With the increase of v^*, the residual strength gradually decreases, indicating that v^* has a weakening effect to the shale, although the data has a discrete type, the mean has a distinct linear relationship and fits it as follows.

$$\lg(\sigma_1 - \sigma_3)^* = -0.061\lg(\mathrm{v}^*) + 2.126, R^2 = 0.974 \quad (8)$$

$$(\sigma_1 - \sigma_3)^* = (v^*)^{-0.0611} + 164.48 \quad (9)$$

Figure 12 shows that with the increase of unloading rate, the mechanical parameters of shale significantly changed, and the residual stress decreased dramatically. The residual stress can reflect the residual strength of the shale reservoir after the geological movement and the hydraulic fracturing during the development process. It is of great significance for the settlement of the site, the deformation of the ground, and the study of the disaster mechanism of shale gas exploration and development.

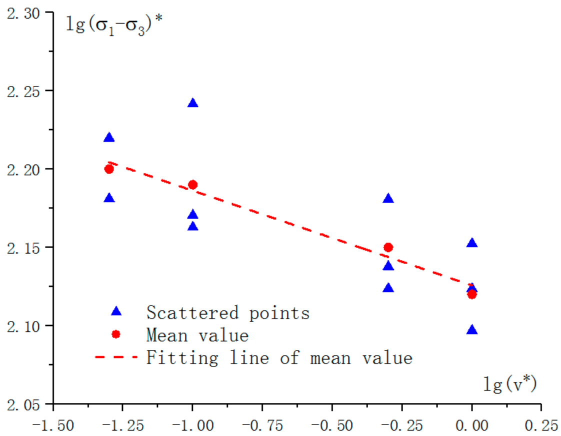

Figure 12. A logarithmic fit curve of residual strength and unloading rate.

3.3. Influence of Unloading Rate on Shale Failure Characteristics

In Figure 13, it shows that the failure modes of the shale triaxial unloading test at different unloading rates, corresponding to the samples in Table 1, which can be concluded that the shale failure pattern and the unloading rate v^* have a great relationship.

When v^* is 0.05 MPa/s, the failure mode of the rock is milder and the damage is more uniform. Based on a typical single bevel shear failure, the shear surface runs through the entire shale, which has visible friction marks.

When v^* is 0.1 MPa/s, the shale fracture morphology began to become complicated. In addition to the oblique section shear failure, fine cracking begins to occur, concentrated on the edge of the shear band. As shown by the arrows in Figure 13b, several tiny cracks perpendicular to the shear band appear and penetrate the entire cleaved surface to form a macroscopic network of cracks. According to the analysis, due to the increase of the unloading rate, the weak structural surface inside the shale sample is opened in the vertical direction under the action of shearing force, forming a small part of local cracking.

When v^* is 0.5 MPa/s, the rupture characteristics tend to be apparent, and the central shear zone still runs through the entire shale sample. At the same time, at the height of one third and one half of the sample, 0°, that is, the crack of the bedding plane occurs. With the further increase of the unloading rate, the bedding plane is also cracked due to the local tension stress resulted from the accelerated rate. There are secondary lateral distribution cracks between the fracture surfaces, and the shale fracture grid tends to be complicated. In the RF-2-5 sample, the sample at the intermediate position, a secondary shear band appears. Although a macroscopic crack is formed, the through slit is not formed.

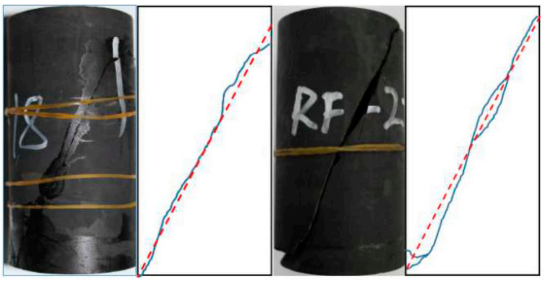

(**a**) 0.05 MPa/s (RF-1-15 and RF-4-11)

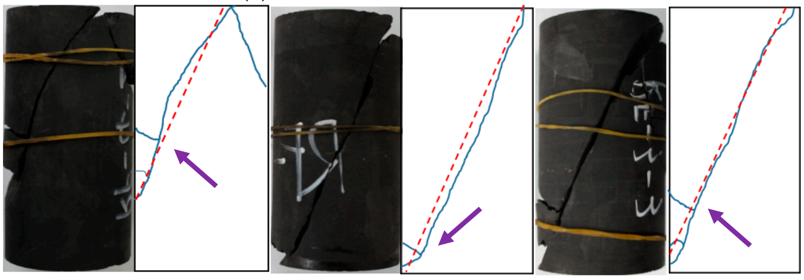

(**b**) 0.1 MPa/s (RF-2-6, RF-4-2 and RF-3-3)

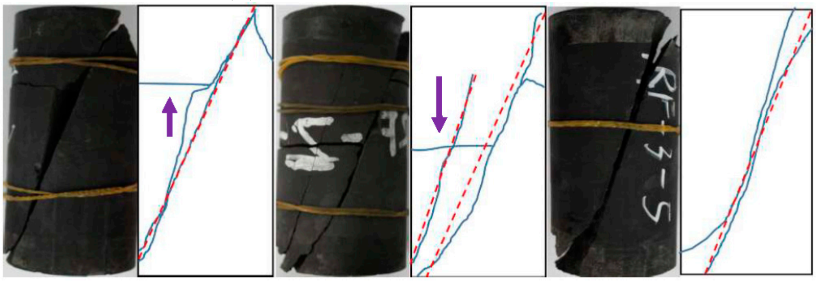

(**c**) 0.5 MPa/s (RF-2-5, RF-3-4 and RF-3-5)

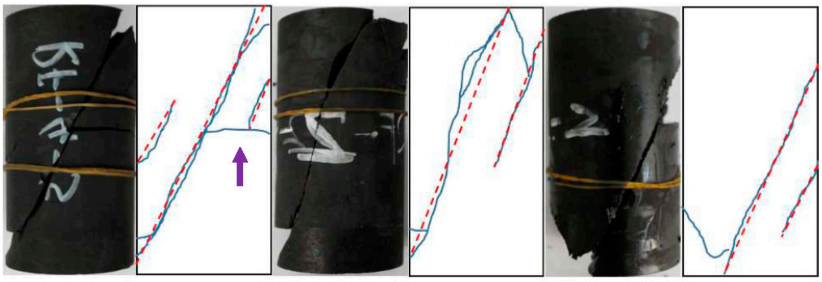

(**d**) 1.0 MPa/s(RF-2-2, RF-4-2, and RF-4-5)

Figure 13. Damage morphologies of shale specimens under different unloading rates.

When v^* is 1.0 MPa/s, with the primary shear zone, the frequency of the secondary non-penetrating shear band increases, and as the unloading rate increases gradually, the weak layer and the structural plane continue to crack, showing the simultaneous shearing of the three shear bands. There are secondary shear bands parallel to the main shear zone, horizontal cracks parallel to the bedding seam, and cracks perpendicular to the primary shear zone. These cracks cause the instability and destruction of the shale as a whole and eventually form a complex fracture network, which quickly leads to the leakage of shale gas during geological changes and affects its exploration and development.

4. Discussion of Rock Brittleness

4.1. Evaluation of Rock Brittleness

The brittleness of shale can significantly affect the stability of the borehole wall and the fracturing effect during on-site development. It is a crucial indicator for evaluating the mechanical properties of the reservoir and is an essential basis for selecting the perforation reconstruction layer and designing the fracturing technology [28]. The establishment of brittleness indicators will help to analyze the brittleness of shale further.

At present, scholars at home and abroad have proposed a variety of methods based on energy, hardness, mineral composition, logging curve, expansion inflection point, pump pressure curve, debris content, fracture toughness, tensile strength ratio, full stress–strain curve, etc. The brittleness evaluation methods are summarized in Table 2 as a total of 33 kinds. Most of their research results are based on their respective research purposes and are used in their respective fields. Based on the stress–strain curve, this paper comprehensively compares several brittleness evaluation methods and attempts to explore their application under unloading conditions.

Hou et al. [27] combine brittleness and stress drop coefficient P, softening modulus M, and brittle drop coefficient R:

$$R = -(\varepsilon_B - \varepsilon_A)/(\varepsilon_M - \varepsilon_A) \tag{10}$$

$$M = (\sigma_a - \sigma_r)/(\varepsilon_A - \varepsilon_B) \tag{11}$$

$$P = (\sigma_a - \sigma_r)/\sigma_a \tag{12}$$

where σ_a represents the peak intensity of the sample at point A, σ_r represents the residual strength of the sample at point B, and ε_A, ε_B, ε_M represent the axial strain of the sample at points A, B, and M, respectively in Figure 14.

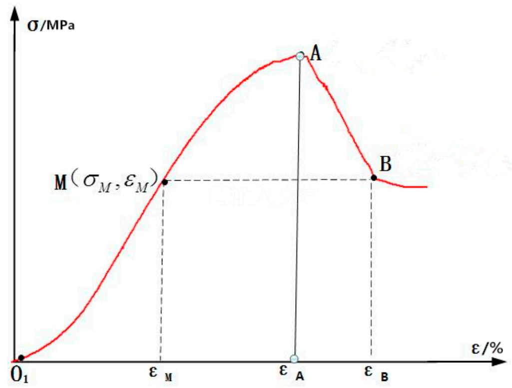

Figure 14. Stress–strain curve of brittle rock [27].

Then the brittleness index B_1, B_2, B_3 are defined, and the normalization is done:

$$B_1 = exp(-R) \tag{13}$$

$$B_2 = (\sigma_a - \sigma_r)/\sigma_a \tag{14}$$

$$B_3 = 1 - exp(M/E) \tag{15}$$

Comprehensive evaluation coefficient B_{d1} and B_{d2} are proposed (i.e., in Table 3):

$$B_{d1} = \alpha B_1 + \beta B_2 + \gamma B_3 \tag{16}$$

$$B_{d2} = B_1 \times B_2 \times B_3 \tag{17}$$

where $\alpha + \beta + \gamma = 1$, α, β, γ represents the weights in the total brittleness index B_1, B_2, B_3, respectively, and can be valued according to the same standard, or may be based on the focus of the project and the different purposes of the research.

Table 2. Research table of brittleness evaluation methods from domestic and foreign scholars.

Method	Equation	Description	Resource
Pressing ratio	$B_1 = \sigma_c \sigma_t / 2$	Mean of the product of uniaxial compressive strength σ_c and tensile strength σ_t.	Altindag [29]
Pressing ratio	$B_2 = (\sigma_c \sigma_t / 2)^{1/2}$	The function of uniaxial compression σ_c and tensile strength σ_t ratio.	Altindag [29]
Pressing ratio	$B_3 = \sigma_c / \sigma_t$	The ratio of uniaxial compressive strength σ_c to tensile strength σ_t.	Hucka and Das [30]
Pressing ratio	$B_4 = (\sigma_c - \sigma_t)/(\sigma_c + \sigma_t)$	The function of uniaxial compression and tensile strength ratio.	Hucka and Das [30]
Hardness test	$B_5 = (H_m - H)/K$	H is the macro hardness and H_m is the micro hardness.	Honda and Sanada [31]
Hardness, fracture test	$B_6 = HE/{K_{IC}}^2$	H is a hardness coefficient, E is Young's modulus, and K_{IC} is the fracture toughness.	J. B. Quinn and G. D. Quinn [32]
Hardness, fracture test	$B_7 = H/K_{IC}$	H is a hardness coefficient, E is Young's modulus, and K_{IC} is the fracture toughness.	Lawn and Marshall [33]
Hardness test	$B_8 = K_{IC}/(\sigma_y h^{1/2})$	K_{IC} is the fracture toughness, σ_y is the yield stress, and h is the characteristic size of the sample.	Bazant and Kazemi [34]
Bazant curve	$B_9 = EG_F/{\sigma_t}^2$	The ratio of elastic energy to fracture energy, G_F is the fracture energy, E is elastic modulus, and σ_t is Hllebrgorg characteristic length value.	Bazant and Kazemi [34]
Cohesion-weakening-friction-strengthening (CWFS) model	$B_{10} = ({\varepsilon_f}^p - {\varepsilon_c}^p)/{\varepsilon_c}^p$	ε_f^p and ε_c^p is the plastic strain when the friction strength and cohesive force reaches the final limit value, respectively.	Hajiabdolmajid et al. [35]
Penetration test	$B_{11} = P_{dec}/P_{inc}$	The ratio of incremental load to decay load.	Copur [36]
Penetration test	$B_{12} = F_{\max}/P$	The ratio of the maximum impact load to the penetration depth.	Yagiz [37]
Impact test	$B_{13} = S_{20}$	Percentage of fine debris less than 11.2 mm in diameter.	Blindheim and Bruland [38]
Impact test	$B_{14} = q\sigma_c$	q is the percentage that less than 0.6 mm of debris and σ_c is uniaxial compressive strength.	Protodyakonov [39]
Mohr stress circle	$B_{15} = \sin\varphi$	Sinusoidal value of internal friction angle.	Hucka and Das [30]
Mohr stress circle	$B_{16} = 45° + \varphi/2$	The function of the internal friction angle.	Hucka and Das [30]
Mineral composition analysis	$B_{17} = (W_{qtz} + W_{carb})/W_{total}$	The ratio of brittle mineral content to total mineral content.	Rickman et al. [40]
Mineral composition analysis	$B_{18} = \frac{w_{qtz}}{w_{total}} \times 100\%$	The ratio of quartz to total mineral content.	Jarvie [41]
Energy dissipation, stress–strain curve	$B_{19} = \frac{dW_r}{dW_e}$	The ratio of rupture energy per unit volume consumption to elastic energy released internally.	Heng et al. [42]
Stress–strain curve	$B_{20} = (\varepsilon_{BRIT} - \varepsilon_n)/(\varepsilon_m - \varepsilon_n) + \alpha CS_{BRIT} + \beta CS_{BRIT} + \eta$	The sum of the peak strain index and the post-peak curve shape index.	Li et al. [43]

Table 2. *Cont.*

Method	Equation	Description	Resource
Stress–strain curve	$B_{21} = W_r/W$	The ratio of recoverable strain energy to total energy.	Hucka and Das [30]
Stress–strain curve	$B_{22} = A_2/A_1$	A_1 is the area under the oblique line of the peak intensity point with the deformation modulus as the slope and A_2 is the area under the loading curve.	Aubertin et al. [44]
Stress–strain curve	$B_{23} = \alpha\sigma_c\varepsilon_f/(\sigma_t\varepsilon_b)$	σ_c is uniaxial compressive strength, σ_t is tensile strength, ε_f and ε_b is a pre-peak and a post-peak strain, respectively, and α is adjustment parameter.	Feng et al. [45]
Stress–strain curve	$B_{24} = \varepsilon_{1i}$	ε_{1i} is an unrecoverable axial strain when the specimen is broken, it is brittle when $\varepsilon_{1i} < 3\%$, brittle plasticity when ε_{1i} at 3%–5%, and plasticity when $\varepsilon_{1i} > 5\%$.	George [46]
Stress–strain curve	$B_{25} = \overline{E} + \overline{\nu}$	The ratio of normalization of elastic modulus and Poisson.	Rickman et al. [40]
Stress–strain curve	$B_{26} = \varepsilon_r/\varepsilon$	The ratio of recoverable strain ε_r to total strain ε.	Hucka and Das [30]
Stress–strain curve, Fracture test	$B_{27} = L{\sigma_t}^2/EG_F$	The ratio of elastic energy to fracture energy, G_F is the fracture energy, E is elastic modulus, and σ_t is characteristic length value.	Bazant and Kazem [34]
Stress–strain curve	$B_{28} = (\tau_p - \tau_r)/\tau_p$	τ_p is the peak strength and τ_r is the residual strength.	Bishop [47]
Stress–strain curve	$B_{29} = (\varepsilon_p - \varepsilon_r)/\varepsilon_p$	The function of is peak strain ε_p and residual strain ε_r.	Ajiabdolmajid and Kaiser [35]
Stress–strain curve	$B_{30} = dW_r/dW_e = (E-M)/M$	The ratio of fracture damage energy to pre-peak elastic strain energy after rock rupture peak.	Stavrogin and Tarasov [48]
Stress–strain curve	$B_{31} = \frac{\tau_p-\tau_r}{\tau_p}\frac{\lg\lvert k_{ac(\mathrm{AC})}\rvert}{10}$	τ_p is the peak strength, τ_r is the residual strength, and $k_{ac(\mathrm{AC})}$ is the slope of different peak intensity points to the drop point, respectively.	Zhou et al. [49]
Stress–strain curve	$B_{32} = \alpha\exp\left[\frac{\varepsilon_B-\varepsilon_A}{(\sigma_r+\sigma_3-2\mu\sigma_3)/\mathrm{E}-\varepsilon_A}\right]$ $+\beta(1-\sigma_r/\sigma_a)+\gamma[1-\exp(\mathrm{M}/\mathrm{E})]$	σ_a is the peak strength, σ_r is the residual strength, ε_A, ε_B, and ε_M are the axial strain and $\alpha+\beta+\gamma=1$.	Hou et al. [27]
Stress–strain curve	$B_{33} = \exp\left[\frac{\varepsilon_B-\varepsilon_A}{(\sigma_r+\sigma_3-2\mu\sigma_3)/\mathrm{E}-\varepsilon_A}\right]$ $\times(1-\sigma_r/\sigma_a)\times[1-\exp(\mathrm{M}/\mathrm{E})]$	σ_a is the peak strength, σ_r is the residual strength, and ε_A, ε_B, and ε_M is the axial strain.	Hou et al. [27]

Table 3. Table of detailed parameters of shale sample brittleness.

Confining Pressure / Parameters	0	20	40	60	80
ε_B	0.76	1.21	1.71	1.86	2.37
ε_A	0.76	1.16	1.53	1.72	1.91
E	11.10	16.09	17.38	18.82	18.83
σ_r	35.58	106.18	149.83	196.79	216.49
σ_3	0.00	20.00	40.00	60.00	80.00
μ	0.24	0.18	0.17	0.21	0.23
σ_A	90.58	162.42	239.33	280.45	306.60
M	−1375.00	−117.17	−52.34	−60.63	−19.34
B_1	1.00	1.01	1.02	1.01	1.04
B_2	0.61	0.35	0.37	0.30	0.29
B_3	1.00	1.00	0.95	0.96	0.64
B_{d1}	0.87	0.78	0.78	0.76	0.66
B_{d2}	0.61	0.35	0.36	0.29	0.20

Combined with the triaxial stress–strain curve of the samples in Figure 5, and when $\alpha = \beta = \gamma = 1/3$ is selected, then the following table can be developed.

It can be seen that the brittleness of the shale sample is well characterized by the brittleness index B_{d1} and B_{d2}, and they decrease continuously with the increase of confining pressure, which plays a proper role in the characterization with the failure of samples in the 3.3-page. Additionally, compared with B_{d1}, the numerical range of B_{d2} is more extensive, and the high brittleness characteristics of shale samples under uniaxial compression can be highlighted, which proves the useful application of the method in triaxial loading test.

4.2. Evaluation of Brittleness during Unloading

4.2.1. Existing Brittleness Evaluation Method

It is equally important to evaluate the brittleness under unloading conditions. The method of the same literature [28] is used to select the peak intensity point A_1 to A_{11}, the residual unloading rate B_1 to B_{11}, the residual intensity point, and the intersection with the elastic section M_1 to M_{11}, which is shown in Figure 15:

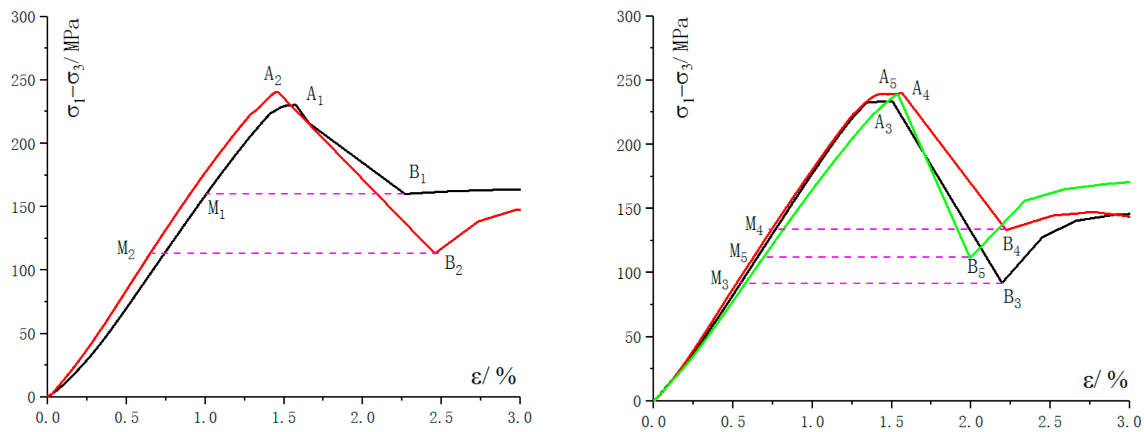

(**a**) Stress–strain curve under the unloading rate of 0.05 MPa/s.

(**b**) Stress–strain curve under the unloading rate of 0.1 MPa/s.

Figure 15. *Cont.*

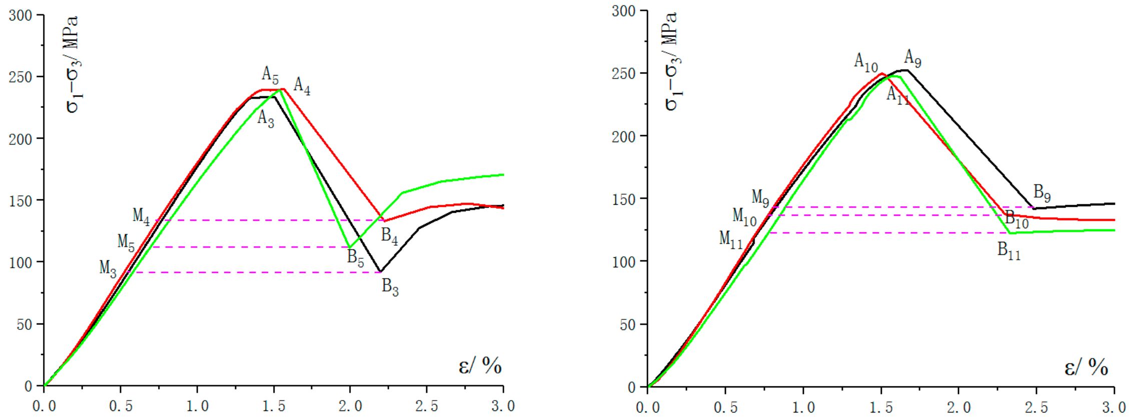

(**c**) Stress–strain curve under the unloading rate of 0.5 MPa/s. (**d**) Stress–strain curve under the unloading rate of 1.0 MPa/s.

Figure 15. Brittleness stress–strain curve of shale samples under different unloading rates.

After a large number of parameter calculations, Table 4 can be obtained. The first row 1–11 of the table corresponds to the 11 unloading curves in Figure 16, and each curve is divided into three points: M, A, and B. Where point A is the peak point of the stress–strain curve, representing the maximum intensity of the pattern at the time of unloading; point B is the brittle drop point, representing the residual intensity after the peak; and point M is the intersection of the parallel line of the point B and the elastic section. Furthermore, σ_A, σ_B, σ_M, respectively correspond to the stress values of points A, B, and M in Figure 16, whose unit is MPa. ε_A, ε_B, ε_M represents the axial strain values of three points: A, B, and M, respectively, whose unit is %. E is the elastic modulus, whose unit is Gpa. μ is the Poisson's ratio, dimensionless. M is softening modulus, dimensionless. B_1, B_2, B_3 are different brittleness indicators, dimensionless. B_d is the comprehensive evaluation coefficient, dimensionless.

Table 4. Evaluation form of shale unloading brittleness index.

No. / Parameters	1	2	3	4	5	6	7	8	9	10	11
σ_A	230.26	240.44	233.42	239.82	238.61	241.51	240.82	246.22	252.00	249.63	247.88
σ_B	160.10	113.15	91.95	133.20	111.36	144.95	116.54	120.80	142.00	137.48	122.59
σ_M	160.10	113.15	91.95	133.20	111.36	144.95	116.54	120.80	142.00	137.48	122.59
ε_A	1.57	1.45	1.51	1.54	1.57	1.45	1.47	1.46	1.67	1.51	1.57
ε_B	2.27	2.46	2.19	2.22	1.99	2.27	2.23	2.03	2.48	2.30	2.33
ε_C	1.01	0.65	0.55	0.74	0.69	0.79	0.71	0.71	0.81	0.77	0.77
E	17.81	17.74	18.44	18.28	16.69	18.52	17.56	18.07	17.35	18.16	17.03
u	0.21	0.27	0.29	0.26	0.27	0.32	0.26	0.25	0.24	0.23	0.25
M	−10.02	−12.60	−20.80	−15.68	−30.30	−11.78	−16.35	−22.00	−13.58	−14.20	−16.49
B_1	1.00	1.00	1.00	1.00	1.00	1.00	1.00	1.00	1.00	1.00	1.00
B_2	0.30	0.53	0.61	0.44	0.53	0.40	0.52	0.51	0.44	0.45	0.51
B_3	0.43	0.51	0.68	0.58	0.84	0.47	0.61	0.70	0.54	0.54	0.62
B_{d1}	0.58	0.68	0.76	0.67	0.79	0.62	0.71	0.74	0.66	0.66	0.71
B_{d2}	0.13	0.27	0.41	0.26	0.45	0.19	0.31	0.36	0.24	0.24	0.31

At four unloading rates, the elastic modulus is relatively close, fluctuating between 16.69 and 18.52, and the average values are 17.78, 17.80, 18.05, and 17.51 GPa, respectively. Poisson's ratio is also relatively close, fluctuating between 0.21 and 0.32, the average values are 0.24, 0.27, 0.28, and 0.24, respectively.

According to the above table, the brittleness index B_{d1} shows a trend of increasing first and then decreasing. The average values at the four unloading rates are 0.63, 0.74, 0.69, and 0.68, respectively, and the brittleness fluctuates significantly under the same unloading rate, such as the unloading rate 0.05 MPa/s, it is 0.58 and 0.68, respectively. The obtained discrete type of B_{d1} is higher, which is inconsistent with the brittleness of the fractured specimen. The brittleness index B_{d2} also shows a trend of increasing first and then decreasing. The average values at the four unloading rates are respectively 0.24, 0.27, 0.28, and 0.24, the gap is small, and the brittleness of shale samples under unloading conditions cannot be characterized. According to the analysis of this paper, the stress path segment from the unloading point to the deviatoric stress is ignored during the calculation, as shown in Figure 16.

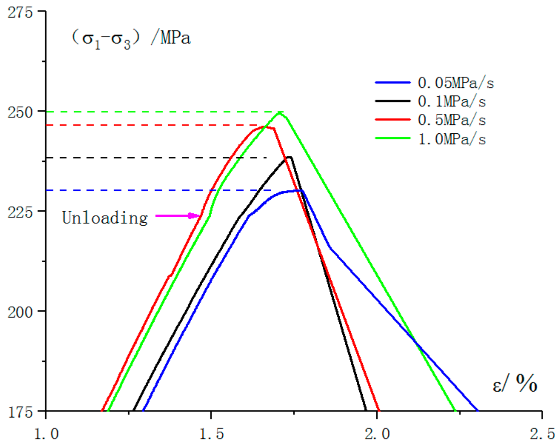

Figure 16. Magnification of typical stress–strain curves for four unloading rates.

Combined with Figure 10, it can be concluded that the unloading stress–strain curve of the 60 MPa confining pressure is between the 40-0 MPa confining pressure of the triaxial loading. The peak intensity during loading is higher, and the curve is dropped faster. When the dropping rate is faster, the axial strain changes are small, the partial stress falls by a significant amount, and the absolute value of the softening modulus M is higher. Under the unloading condition, the peak strength of the shale is reduced obviously, the residual strength of the unloading is also reduced, and the curve drop rate is also weakened, which shows that the absolute value of the softening modulus M is lower. That is, under the unloading conditions, the M value cannot accurately reflect the softening modulus of the sample. Moreover, the brittleness index evaluation method in [27] only considers the deformation modulus E in the elastic deformation stage, and does not take into account the deformation modulus change after the unloading point. Therefore, the method is suitable for the triaxial loading test and does not apply to the evaluation of rock brittleness at different unloading rates with the same confining pressure.

4.2.2. Proposal of Brittleness Evaluation Method Considering Unloading Conditions

Aiming at the above problems, the author proposes a brittleness evaluation method based on the unloading stress–strain curve. This method can consider the influence of different unloading rates on shale brittleness characteristics under the same confining pressure condition, and can be related to reservoir geology to analyze the brittleness of the reservoir further, providing a basis for the mining of preferred high brittle blocks and hydraulic fracturing.

After the unloading point in Figure 16, the magnitude of the deviatoric stress changes significantly at different unloading rates. Therefore, let the unloading point be U, them the unloading deformation modulus E_U is proposed, which is taken from the amount of change between the deviatoric stress and the axial strain, between the peak point A and the unloading point U, that is, the discontinuous line at the unloading point in Figure 17 to the discontinuous line at the peak of the respective rate, which is:

$$E_U = (\sigma_A - \sigma_U)/(\varepsilon_A - \varepsilon_U) \tag{18}$$

where σ_A, σ_U represents the intensity of the unloading point A and the peak point U, respectively, and ε_A, ε_U represents the axial deformation of the point A and the point U, respectively. By calculation, the following table can be obtained (the sample number in the table omits the previous RF).

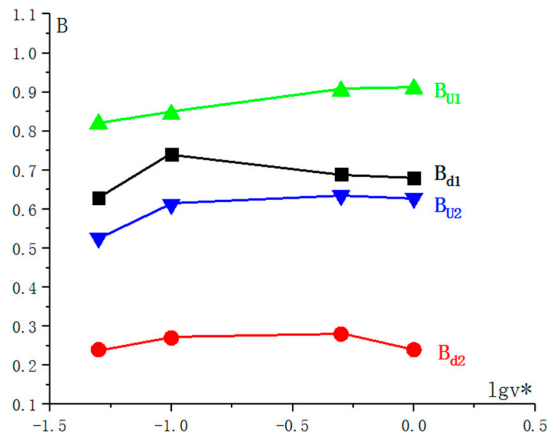

Figure 17. Comparison of the methods.

As the unloading rate increases in Table 5, there is a significant increase from the lowest of 15.74 to 65.38 GPa in E_U. Therefore, the total elastic modulus based on both loading and unloading is proposed:

$$E_T = \phi E + \gamma E_U \tag{19}$$

where E_T is the total elastic modulus that considered both the loading and unloading, E is the elastic modulus of the elastic section before the unloading point, E_U is the unloading elastic modulus, ϕ and γ are the composite coefficient, and $\phi + \gamma = 1$. Then the Equation (18) is substituted into (19), and Equation (20) can be got.

$$E_T = \phi E + \gamma(\sigma_A - \sigma_M)/(\varepsilon_A - \varepsilon_M) \tag{20}$$

Table 5. Unloading elastic modulus parameter table.

No.	1-15	4-11	2-7	3-3	4-2	2-5	3-4	3-5	2-2	2-9	4-5
E_U/GPa	15.74	38.73	22.59	26.50	41.25	44.90	58.40	50.50	42.68	65.38	52.60

Because M and E are covered by B_3 in the literature [28] and E is also covered in B_1, B_1, B_2 and B_3 are not independent. So they cannot be fitted to B_{d1} and B_{d2}, then B_3 is deleted and E_T is imported, and the brittleness evaluation index B_{U1} and B_{U2}, which consider the loading and unloading part, can be established.

$$B_{U1} = \alpha \cdot exp\left\{\frac{[\phi E + \gamma(\sigma_A - \sigma_M)/(\varepsilon_A - \varepsilon_M)] \times (\varepsilon_B - \varepsilon_A)}{\sigma_r + \sigma_3 - 2\mu\sigma_3 - [\phi E + \gamma(\sigma_A - \sigma_M)/(\varepsilon_A - \varepsilon_M)]\varepsilon_A}\right\} + \beta \cdot (1 - \frac{\sigma_r}{\sigma_A}) \tag{21}$$

$$B_{U2} = exp\left\{\frac{[\phi E + \gamma(\sigma_A - \sigma_M)/(\varepsilon_A - \varepsilon_M)](\varepsilon_B - \varepsilon_A)}{\sigma_r + \sigma_3 - 2\mu\sigma_3 - [\phi E + \gamma(\sigma_A - \sigma_M)/(\varepsilon_A - \varepsilon_M)]\varepsilon_A}\right\} \times (1 - \frac{\sigma_r}{\sigma_A}) \tag{22}$$

where $\phi + \gamma = 1$, $\alpha + \beta = 1$, the value of ϕ and γ can fully consider the size of the unloading rate and the difference of the unloading point and the value of α and β can measure the different effects of stress and strain on the brittleness. Under the same confining pressure condition, σ_3 is generally a fixed value, E is the elastic modulus of the elastic section before the unloading point, μ is the Poisson's ratio of the pattern, and the remaining parameters can be read in the stress–strain curve.

4.2.3. Verification of the Brittleness Method and Comparison with Others

In the unloading test of this paper, due to the discrete difference of some samples, it has a small range of fluctuations of E, but E_U has a more significant influence on the peak strength and brittleness of the unloading, so ϕ is taken as 0.4 and γ is taken as 0.6, which are more suitable for the actual situation during unloading. Then α and β are both taken as 0.5, and E_T can be calculated, as shown in Table 6.

Table 6. Table of total elastic modulus.

No.	1-15	4-11	2-7	3-3	4-2	2-5	3-4	3-5	2-2	2-9	4-5
E_T/GPa	16.57	30.33	20.93	23.21	31.43	34.35	42.06	37.53	32.55	46.49	38.37

Then E_T can be substituted into Equations (21) and (22), and the brittleness index B_{U1} and B_{U2} can be got.

From the comparison of the new methods and Hou's method in Figure 17 and Table 7, we can easily obtain that there are fluctuations between B_{U1} and B_{U2}, which means they cannot characterize the brightness of the shale during the unloading. The average value of B_{U1} and B_{U2} can be calculated and obtained at each unloading rate, the average values of B_{U1} at 0.05, 0.1, 0.5, and 1.0 MPa/s are: 0.819, 0.843, 0.903, and 0.909, respectively. It has a good brittleness characterization with the unloading damage and parameter changes in Chapter 3, and the feasibility of the brittleness evaluation method is verified. The average values of B_{U2} at 0.05, 0.1, 0.5, and 1.0 MPa/s are 0.526, 0.612, 0.635, and 0.628. As the unloading rate increases, the overall trend of B_{U2} shows an upward trend and there is a small fluctuation at the unloading rate of 1.0 MPa/s. B_{U2} can also characterize the rock sample at different unloading rates, but it is weaker than the characterization of B_{U1}.

Table 7. Table of the brittleness indicator parameter.

No.	1-15	4-11	2-7	3-3	4-2	2-5	3-4	3-5	2-2	2-9	4-5
B_{U1}	0.688	0.950	0.893	0.789	0.846	0.836	0.993	0.880	0.842	0.947	0.937
B_{U2}	0.326	0.725	0.716	0.504	0.617	0.508	0.759	0.637	0.545	0.649	0.692

5. Conclusions

In this paper, the axial compression loading and confining pressure unloading test is carried out under the confining pressure of 60 MPa. The relationship between the unloading rate and the mechanical characteristics of the shale is discussed, also the brittleness of shale under the unloading path are analyzed. The following conclusions are obtained:

(1) With the increase of unloading rate v^*, the axial strain and radial strain increases, the radial strain is more significant, and the volumetric strain is reduced gradually, which shows that the dilatancy is weaker. The unloading rate has a strengthening effect on the peak deviatoric stress and has a weakening effect on the residual deviatoric stress and the confining pressure, and there is a typical linear relationship between them. The modulus of elasticity decreases and the logarithm of the peak intensity has a significant linear relationship with the logarithm of the strain rate.

(2) When v^* is 0.05 MPa/s, the shale failure mode is mild, which is a typical single slope shear failure. When v^* is 1.0 MPa/s, the shale fracture morphology is more complicated, the shear fracture surface is increased, and some bedding surface cracks. There are fine vertical distribution cracks between the fracture surfaces, and the shale fracture is sufficient, which shows the simultaneous development of multiple shear zones and synchronous cracking inside the layers, resulting in the overall instability of the shale.

(3) The brittleness evaluation methods are summarized as a total of 33 kinds, and the brittleness of shale samples is well characterized by the brittleness index B_{d1} and B_{d2} during the loading process, they decrease continuously with the increase of confining pressure, which plays a good role in the characterization of the uniaxial failure and the triaxial failure. What is more, compared with B_{d1}, the numerical range of B_{d2} is larger, and the high brittleness characteristics of shale

samples under uniaxial compression can be highlighted, which proves the effective application of the method in triaxial loading test.

(4) Aiming at the shortage of B_{d1} and B_{d2} during the unloading process, this paper proposes a brittleness evaluation method based on the unloading stress–strain curve, which can consider the influence of different unloading rates, and there is a good brittleness characterization between the unloading damage and parameter changes of B_{U1} and B_{U2}. This can be related to reservoir geology to analyze the brittleness of the reservoir further, providing a basis for the mining of preferred high brittle blocks and hydraulic fracturing.

The following research will continue to focus on the unloading rate, explore the shale unloading test at different bedding angles under different confining pressure conditions, and deeply explore the shale unloading mechanism.

Author Contributions: Conceptualization, X.Z., H.L. and Y.G.; data curation, X.Z. and L.W.; formal analysis, X.Z.; funding acquisition, H.L., Y.G. and L.W.; investigation, Z.H. and P.D.; project administration, H.L., Y.G. and L.W.; resources, H.L., Y.G. and L.W.; supervision, H.L. and Y.G.; validation, X.Z., Z.H. and P.D.; writing—original draft, X.Z.; writing—review and editing, X.Z., H.L., Y.G., L.W., Z.H. and P.D.

Funding: The research was funded by the National Natural Science Foundation of China (51574218, 51764020), National Science and Technology Major Project of China (2017ZX05036-003-004), National Key Research and Development Plan (2018YFC0808403, 2017YFC0804601), and Research on Key Scientific and Technical Issues in Exploration and Development of Shale Gas (XDB10040200), CAS pilot project (B). We would like to express our greatest gratitude for their generous support.

Conflicts of Interest: The authors declare no conflicts of interest.

Nomenclature

ε_1	Axial strain, mm/mm
ε_2	Radial strain, mm/mm
ε_v	Volumetric strain, mm/mm
σ_1	Major principal stress, MPa
σ_3	Confining pressure, MPa
$\sigma_1 - \sigma_3$	Axial pressure, MPa
k	Strength coefficient, -
b	Strength coefficient, -
φ	Internal friction angle, °
c	Cohesion, MPa
v^*	Unloading rate, MPa/s
$\lg(v^*)$	The logarithm of unloading rate, -
$(\sigma_1 - \sigma_3)_{\max}$	Maximum axial pressure, MPa
$\lg((\sigma_1 - \sigma_3)_{\max})$	The logarithm of maximum axial pressure, -
$(\sigma_1 - \sigma_3)^*$	Residual stress, MPa
$\lg((\sigma_1 - \sigma_3)^*)$	The logarithm of residual stress, -
σ_3^*	Failure confining pressure, MPa
$\lg\sigma_3^*$	The logarithm of failure confining pressure, -
P	Stress drop coefficient, -
M	Softening modulus, -
R	Brittle drop coefficient, -
σ_a	The peak intensity of the sample at point A, MPa
σ_r	Residual strength of the sample at point B, MPa
ε_A	Axial strain of the sample at points A, %
ε_B	Axial strain of the sample at points B, %
ε_M	Axial strain of the sample at points M, %
ε_U	Axial strain of the sample at points U, %
B_1	Brittleness index, -
B_2	Brittleness index, -
B_3	Brittleness index, -

B_{d1}	Evaluation coefficient, -
B_{d2}	Evaluation coefficient, -
σ_A	Stress values of point A, MPa
σ_B	Stress values of point B, MPa
σ_M	Stress values of point M, MPa
σ_U	Stress values of point U, MPa
E	Elastic modulus, GPa
μ	Poisson's ratio, -
α	Weights coefficient, -
β	Weights coefficient, -
γ	Weights coefficient, -
E_T	Total elastic modulus, GPa
E_U	Unloading elastic modulus, GPa
ϕ	Composite coefficient, -
γ	Composite coefficient, -
B_{U1}	Brittleness evaluation index, -
B_{U2}	Brittleness evaluation index, -

References

1. Guo, X.S. Rules of two-factor enrichment for marine shale gas in Southern China—Understanding from the Longmaxi formation shale gas in Sichuan basin and its surrounding area. *Acta Geol. Sin.* **2014**, *88*, 1209–1218. (In Chinese) [CrossRef]
2. Lyu, Q.; Ranjith, P.G.; Long, X.P.; Ji, B. Experimental investigation of mechanical properties of black shales after CO2-water-rock interaction. *Materials* **2016**, *9*, 663. [CrossRef] [PubMed]
3. Kim, K.; Choe, J. Hydraulic Fracture Design with a Proxy Model for Unconventional Shale Gas Reservoir with Considering Feasibility Study. *Energies* **2019**, *12*, 220. [CrossRef]
4. Energy Information Administration. Shale Gas Production Drives World Natural Gas Production Growth. 2016. Available online: https://www.eia.gov/todayinenergy/detail.php?id=27512 (accessed on 15 August 2016).
5. Huo, L.; Yang, C.H.; Liu, J.X.; Mao, H.J.; Huang, W.G. Experimental research on the failure of mudstone cap rock of Western Hubei-Eastern Chongqing suffered uplift and erosion. *Chin. J. Undergr. Space Eng.* **2018**, *14*, 33–42. (In Chinese)
6. Huo, L.; Yang, C.H.; Mao, H.J.; Liu, J.X.; Yuan, X.S. Experimental research on mechanical properties of western Hubei-Eastern Chongqing carbonaceous shale cap rock under unloading stress path. *Chin. J. Rock Mech. Eng.* **2016**, *a0135*, 2898–2906. (In Chinese) [CrossRef]
7. Cao, C.R.; Han, C.H.; Zheng, D.R. Impact of structural changes on reservoir preservation. *Mar. Geol. Quat. Geol.* **2003**, *23*, 95–98. (In Chinese) [CrossRef]
8. Li, J.Q.; Gao, Y.Q.; Hua, C.X.; Xia, Z.L. Enlightenment from the experience of shale gas exploration in North America to the establishment of an evaluation system for marine shale gasification area in South China. *Pet. Geol. Recovery Effic.* **2014**, *21*, 23–27. (In Chinese) [CrossRef]
9. Dewhurst, D.N.; Hennig, A.L. Geomechanical properties related to top seal leakage in the Carnarvon Basin, Northwest Shelf, Australia. *Pet. Geosci.* **2003**, *9*, 255–263. [CrossRef]
10. Lewis, H.; Olden, P.; Couples, G.D. Geomechanical simulations of top seal integrity. *Nor. Pet. Soc. Spec. Publ.* **2002**, *11*, 75–87. [CrossRef]
11. Hermanrud, C.; Bols, H.M.; Teige, G.M. Seal failure related to basin-scale processes. *AAPG Hedberg Series* **2005**, *1975*, 13–22. [CrossRef]
12. Teige, G.M.; Hermanrud, C.; Kløvjan, O.S.; Eliassen, P.E.; Løseth, H.; Gading, M. Evaluation of caprock integrity in the western (high-pressured) haltenbanken area—A case history based on analyses of seismic signatures in overburden rocks. *Nor. Pet. Soc. Spec. Publ.* **2002**, *11*, 233–242. [CrossRef]
13. Ogata, K.; Senger, K.; Braathen, A.; Tveranger, J. Fracture corridors as seal-bypass systems in siliciclastic reservoir-cap rock successions: Field-based insights from the Jurassic Entrada Formation (SE Utah, USA). *J. Struct. Geol.* **2014**, *66*, 162–187. [CrossRef]
14. Shukla, R.; Ranjith, P.G.; Choi, S.K.; Haque, A.; Yellishetty, M.; Hong, L. Mechanical behaviour of reservoir rock under brine saturation. *Rock Mech. Rock Eng.* **2013**, *46*, 83–93. [CrossRef]

15. Ingram, G.M.; Urai, J.L. Top-seal leakage through faults and fractures: The role of mudrock properties. *Geol. Soc. Lond. Spec. Publ.* **1999**, *158*, 125–135. [CrossRef]
16. Swansson, S.R.; Brown, W.S. An observation of loading path independence of fracture in rock. *Int. J. Rock Mech. Min. Sci. Geomech. Abstr.* **1971**, *8*, 277–281. [CrossRef]
17. Shimamoto, T. Confining pressure reduction experiments: A new method for measuring frictional strength over a wide range of normal stress. *Int. J. Rock Mech. Min. Sci. Geomech. Abstr.* **1985**, *22*, 227–236. [CrossRef]
18. Viktorov, S.D.; Kochanov, A.N. Investigation into the processes of rock sample unloading after blast loading. *J. Min. Sci.* **2004**, *40*, 160–164. [CrossRef]
19. Lau, J.S.O.; Chandler, N.A. Innovative laboratory testing. *Int. J. Rock Mech. Min. Sci.* **2004**, *41*, 1427–1445. [CrossRef]
20. Huang, R.Q.; Huang, D. Experimental research on affection laws of unloading rates on mechanical properties of Jinping marble under high geostress. *Chin. J. Rock Mech. Eng.* **2010**, *29*, 21–33. (In Chinese)
21. Huang, X.; Liu, Q.S.; Liu, B.; Liu, X.W.; Pan, Y.C.; Liu, J.P. Experimental study on the dilatancy and fracturing behavior of soft rock under unloading conditions. *Int. J. Civ. Struct. Eng.* **2017**, *15*, 1–28. [CrossRef]
22. Zhang, L.M.; Wang, Z.Q.; Shi, L. Experimental study of hard rock failure characteristic under unloading condition. *Chin. J. Rock Mech. Eng.* **2011**, *30*, 1230–1236. (In Chinese) [CrossRef]
23. Lv, Y.H.; Liu, Q.S.; Jiang, H. Study of mechanical deformation characteristics of granite in unloading experiments of high stress. *Rock Soil Mech.* **2010**, *31*, 337–344. (In Chinese) [CrossRef]
24. Wu, F.Q.; Liu, J.Y.; Liu, T.; Zhuang, H.Z.; Yan, C.G. A method for assessment of excavation damaged zone (EDZ) of a rock mass and its application to a dam foundation case. *Eng. Geol.* **2009**, *104*, 254–262. [CrossRef]
25. He, M.C.; Miao, J.L.; Feng, J.L. Rock burst process of limestone and its acoustic emission characteristics under true-triaxial unloading conditions. *Int. J. Rock Mech. Min. Sci.* **2010**, *47*, 286–298. [CrossRef]
26. Hatheway, A.W. The complete ISRM suggested methods for rock characterization, testing, and monitoring: 1974–2006. *Environ. Eng. Geol.* **2009**, *15*, 47–48. [CrossRef]
27. Hou, Z.K.; Yang, C.H.; Wei, X.; Wang, L.; Wei, Y.L.; Xu, F.; Wang, H. Experimental study on the brittle characteristics of Longmaxi formation shale. *J. China Coal Soc.* **2016**, *41*, 1188–1196. (In Chinese) [CrossRef]
28. Hou, Z.K.; Yang, C.H.; Wang, L.; Xu, F. Evaluation Method of Shale Brittleness Based on Indoor Experiments. *J. Northeast. Univ. Nat. Sci.* **2016**, *37*, 1496–1501. (In Chinese) [CrossRef]
29. Altindag, R. The evaluation of rock brittleness concept on rotary blast hold drills. *J. S. Afr. Inst. Min. Metall.* **2002**, *102*, 61–66.
30. Hucka, V.; Das, B. Brittleness determination of rocks by different methods. *Int. J. Rock Mech. Min. Sci. Geomech. Abstr.* **1974**, *11*, 389–392. [CrossRef]
31. Honda, H.; Sanada, Y. Hardness of coal. *Fuel* **1956**, *35*, 451–461.
32. Quinn, J.B.; Quinn, D.G. Indentation brittleness of ceramics: A fresh approach. *J. Mater. Sci.* **1997**, *32*, 4331–4346. [CrossRef]
33. Lawn, B.; Marshall, D. Hardness, toughness, and brittleness: An indentation analysis. *J. Am. Ceram. Soc.* **1979**, *62*, 347–350. [CrossRef]
34. Azant, Z.P.; Kazemi, M.T. Determination of fracture energy, process zone length and brittleness number from size effect, with application to rock and concrete. *Int. J. Fract.* **1990**, *44*, 111–131. [CrossRef]
35. Hajiabdolmajid, V.; Kaiser, P. Brittleness of rock and stability assessment in hard rock tunneling. *Tunn. Undergr. Space Eng.* **2003**, *18*, 35–48. [CrossRef]
36. Copur, H. Theoretical and Experimental Studies of Rock Cutting with Drag Bits Toward the Development of a Performance Prediction Model for Roadheaders. Ph.D Thesis, Colorado School of Mines, Golden, CO, USA, 1999.
37. Yagiz, S. An investigation on the relationship between rock strength and brittleness. In Proceedings of the 59th Geological Congress of Turkey, Ankara, Turkey, 20–24 March 2006; MTA General Directory Press: Ankara, Turkey, 2006.
38. Blindheim, O.T.; Bruland, A. Boreability testing. *Nor. TBM Tunn.* **1998**, *30*, 29–34.
39. Protodyakonov, M.M. Mechanical properties and drillability of rocks. In Proceedings of the 5th Symposium Rock Mechanics, University of Minnesota, Minneapolis, MN, USA, May 1962.
40. Rickman, R.; Mullen, M.J.; Petre, J.E.; Grieser, W.V.; Kundert, D. A practical use of shale petrophysics for stimulation design optimization: All shale plays are not clones of the Barnett Shale. In Proceedings of the

SPE Annual Technical Conference and Exhibition, Denver, CO, USA, 21–24 September 2008; Society of Petroleum Engineers: Denver, CO, USA, 2008.
41. Jarvie, D.M.; Hill, R.J.; Ruble, T.E.; Pollastro, R.M. Unconventional shale-gas systems: The Mississippian Barnett Shale of north-central Texas as one model for thermogenic shale-gas assessment. *AAPG Bull.* **2007**, *91*, 475–499. [CrossRef]
42. Heng, S.; Yang, C.H.; Li, Z.; Wang, L.; Hou, Z.K. Shale brittleness estimation based on energy dissipation. *J. Cent. South Univ. Nat. Sci.* **2016**, *47*, 577–585. (In Chinese) [CrossRef]
43. Li, Q.H.; Chen, M.; Jin, Y.; Wang, F.P.; Hou, B.; Zhang, B.W. Indoor evaluation method for shale brittleness and improvement. *Chin. J. Rock Mech. Eng.* **2012**, *31*, 1680–1685. (In Chinese)
44. Aubertin, M.; Gill, D.E.; Simon, R. On the use of the brittleness index modified (BIM) to estimate the post-peak behavior of rocks. In Proceedings of the 1st North American Rock Mechanics Symposium, Austin, TX, USA, 1–3 June 1994; American Rock Mechanics Association: Austin, TX, USA, 1994.
45. Feng, T.; Xie, X.B.; Wang, W.X.; Pan, C.L. Brittleness of rock and brittleness coefficient describing rockburst tendency. *Min. Metall. Eng.* **2000**, *20*, 18–19. (In Chinese)
46. George, E.A. Brittle failure of rock material-test results and constitutive models. *AA Balkema/Rotterdam/Brolkfield* **1995**, *2*, 123–128. [CrossRef]
47. Bishop, A.W. Progressive failure with special reference to the mechanism causing it. *Proc. Geotech. Conf. Oslo* **1967**, *2*, 142–150.
48. Stavrogin, A.N.; Tarasov, B.G. *Experimental Physics and Rock Mechanics*; CRC Press: Boca Raton, FL, USA, 2001.
49. Zhou, H.; Meng, F.Z.; Zhang, C.Q.; Xu, R.C.; Lu, J.J. Quantitative evaluation of rock brittleness based on stress–strain curve. *Chin. J. Rock Mech. Eng.* **2014**, *33*, 1114–1122. (In Chinese) [CrossRef]